ICC 2022 - IEEE International Conference on Communications | 978-1-5386-8347-7/22/$31.00 ©2022 IEEE | DOI: 10.1109/ICC45855.2022.9838634

On the Performance Bound of Multi-Agent Formation with Localization Uncertainty

Kai Ma, Jian Wang, Yu Wang and Yuan Shen
Tsinghua National Laboratory for Information Science and Technology
Department of Electronic Engineering, Tsinghua University, Beijing 100084, China
Email: mk19@mails.tsinghua.edu.cn, {jian-wang, yu-wang, shenyuan_ee}@tsinghua.edu.cn

***Abstract*—Multi-agent systems are being widely deployed to various tasks due to excellent collaboration gains. These tasks usually contain localization and control stages, in which the information coupling mechanism is still unclear thus many system resources are wasted. In this paper, we integrally analyze the performance bound of 3D formation accuracy with localization uncertainty so as to reduce consumption. We start from the equivalence class distance to analyze the 3D relative formation distance and obtain its closed-form upper bound and lower bound. Then we establish an integrated localization and control framework for the 3D formation and analyze how observation and control errors affect the formation accuracy. We propose integrated feedback resource allocation algorithms including agents scheduling and power allocation. Simulation results show the significant performance gain and resource cost reduction brought by the integrated framework.**

***Index Terms*—collaborative system; integrated localization and control; formation control; resource allocation**

I. Introduction

Multi-agent cooperative systems are attracting great attention from the academic and industrial communities. Excellent collaboration gains bring huge application scenarios to the multi-agent systems. In collaborative tasks, such as detection [1], surveying [2], and target tracking [3], the position accuracy of formations is an important factor affecting the performance. The formation accuracy consists of the absolute accuracy of the formation center and the relative accuracy between agents, where the latter is more concerned [4]. Usually, we are more tolerant of the translation or rotation deviation of the whole formation, but more strict with the accuracy of the relative structures which directly affects collaboration gains.

There are usually two ways to measure the error of relative formations. One way is based on the rigid theory, using the sum of errors on each side and each angle [5]. This metric has a simple form and is convenient to design control algorithms, but it is hard to analyze the noise coupling relationship from localization to formation control. In addition, the weighted sum between the distance errors and the angle errors lacks physical meanings. The other way is to use the quotient distance as a metric, i.e. the minimum Euclidean distance between two formations under the equivalence of translation and rotation [6], [7]. It has a clear physical meaning and provides a way to analyze the coupling mechanism of localization and control. In this paper, we use the latter metric.

Since there is a natural information coupling between localization and formation control as shown in Fig. 1, the constrained resources can be used more effectively under integrated frameworks [7]–[9]. On the one hand, the integrated design can provide better control strategies based on available measurements. On the other hand, the system can allocate measurement resources more appropriately guided by integrated tasks. However, most localization algorithms ignore the need for formation control, and most formation control algorithms ignore the localization uncertainty and simply assume that all the agent positions are accurate [4], [10], [11]. Some scholars jointly designed the localization and control algorithms directly from the measurement information [3], [8], but they lack analysis of the internal coupling mechanism. Some scholars theoretically analyzed an integrated localization and control framework for the 2D relative formation and they verify that the joint design has significant gains [7], but this framework can not be trivially expanded to the 3D relative formation, since the three-dimensional rotation group $\mathrm{SO}(3)$ lacks many good properties that are only established in the two-dimensional rotation group $\mathrm{SO}(2)$.

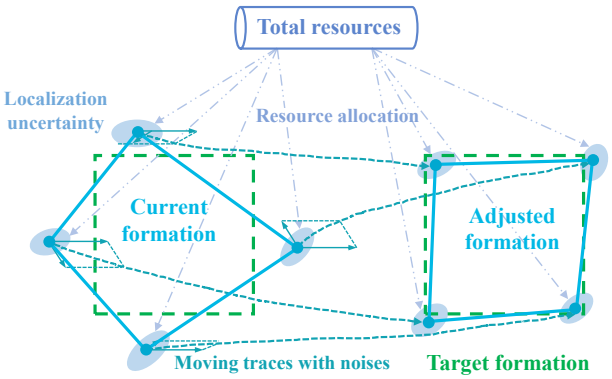

Fig. 1. Sketch map of localization and formation problems. The agents estimate the current formation and design control strategies to close the target formation, where the moves include the consensual absolute moves and the relative moves to adjust relative structure. Proper resource allocation can more effectively reduce localization errors of key agents.

In this paper, we propose an integrated localization and control framework for the 3D formation and analyze the relative formation error bound under any unbias control algorithm. Based on the theoretical analysis, we propose resource feedback allocation strategies, which can significantly reduce resource consumption without reducing the formation accuracy.

Notations: Vectors and matrices are written as bold italic letters $\boldsymbol{x}$ and bold capital italic letters $\boldsymbol{X}$, respectively. $\boldsymbol{I}$ is the identity matrix of the appropriate dimension. $\mathbf{1}_N$ is the N-dimensional column vector with all elements being 1. $[\cdot]^{\mathrm{T}}$, $[\cdot]^{-1}$ and $\mathrm{tr}\{\cdot\}$ denote the transpose, inverse and trace of its argument, respectively. $\otimes$ denotes the Kronecker product. $\dim(V)$ is the dimension of V and $\mathrm{span}(V)$ is the set of all linear combinations of V.

II. System Model

A. Formation Error

In this paper, we discuss the problem of multi-agent formation in three-dimensional space. The state space of agent i is modeled as $\boldsymbol{x}_i = [x_i, y_i, z_i]$, where x_i, y_i, and z_i are the position coordinates. The state space of a formation composed of N agents at time k is defined as

$$\boldsymbol{x}^{(k)} = [\boldsymbol{x}_1^{(k)\mathrm{T}}, \boldsymbol{x}_2^{(k)\mathrm{T}}, \ldots, \boldsymbol{x}_N^{(k)\mathrm{T}}]^{\mathrm{T}}. \tag{1}$$

Denote the target formation as $\boldsymbol{\xi} \in \mathbb{R}^{3N}$. In the relative formation problem, if another N-agent formation $\boldsymbol{s}$ can be transformed from the formation $\boldsymbol{\xi}$ by rotation transformations and/or translation transformations, we say they are equivalent. The set of all the formations equivalent to $\boldsymbol{\xi}$, the equivalence class of $\boldsymbol{\xi}$, can be expressed as $\mathcal{F}_{\boldsymbol{\xi}} \triangleq \{\boldsymbol{s} : \boldsymbol{s} = (\boldsymbol{I} \otimes \boldsymbol{R})\boldsymbol{\xi} + \boldsymbol{I} \otimes \boldsymbol{k}, \boldsymbol{R} \in \mathrm{SO}(3), \boldsymbol{k} \in \mathbb{R}^3\}$, where $\boldsymbol{R}$ is a 3D rotation matrix and $\boldsymbol{k}$ is a 3D translation vector.

We define the formation error between the actual formation $\boldsymbol{x}$ and the target formation $\boldsymbol{\xi}$ as the minimum square distance between their corresponding equivalence classes, i.e.

$$d(\boldsymbol{\xi}, \boldsymbol{x}) \triangleq \min_{\boldsymbol{s} \in \mathcal{F}_{\boldsymbol{\xi}}, \boldsymbol{t} \in \mathcal{F}_{\boldsymbol{x}}} \|\boldsymbol{s} - \boldsymbol{t}\|^2. \tag{2}$$

In fact, this is the quotient square distance of Euclidean square distance under the translation and rotation equivalence. Due to the reversibility of translation and rotation, (2) has the following equivalent form

$$d(\boldsymbol{\xi}, \boldsymbol{x}) = \min_{\boldsymbol{t} \in \mathcal{F}_{\boldsymbol{x}}} \|\boldsymbol{\xi} - \boldsymbol{t}\|^2 = \min_{\boldsymbol{s} \in \mathcal{F}_{\boldsymbol{\xi}}} \|\boldsymbol{s} - \boldsymbol{x}\|^2. \tag{3}$$

Due to observation noise and control noise, we can neither obtain the true position of agents nor accurately control agents, so the actual formation is a random vector. Here we define the mean formation error as $E\{d(\boldsymbol{\xi}, \mathbf{x})\}$, to describe the error between a random formation $\mathbf{x}$ and the target formation $\boldsymbol{\xi}$.

B. Measurement and Control Model

At time k, agents obtain measurement information which is a random vector $\mathbf{y}^{(k)} \sim p_{\mathbf{y}}(\mathbf{y}; \boldsymbol{x}^{(k)}, \mathcal{R})$, where $\mathcal{R}$ is the resource strategy such as energy allocation and scheduling priority. The Fisher information matrix of measurements is denoted as $\boldsymbol{J}(\boldsymbol{x}^{(k)}) = \mathbb{E}[\frac{\partial \ln p(\mathbf{y}; \boldsymbol{x}^{(k)}, \mathcal{R})}{\partial \boldsymbol{x}^{(k)}} \frac{\partial \ln p(\mathbf{y}; \boldsymbol{x}^{(k)}, \mathcal{R})}{\partial \boldsymbol{x}^{(k)\top}}]$.

For any agent i, its move can be decomposed into two parts, the absolute move $\boldsymbol{u}$ which should be consistent with the formation center, and the relative move $\boldsymbol{c}_i$ which is relative to other agents (as shown in Fig. 1). The state equation of agent i is expressed as

$$\boldsymbol{x}_i^{(k+1)} = \boldsymbol{x}_i^{(k)} + \boldsymbol{u}^{(k)} + \boldsymbol{c}_i^{(k)} + \mathbf{w}_i^{(k)}, \tag{4}$$

where $\mathbf{w}_i^{(k)}$ is the control noise at time k. Assume all the noises are independent. The total state equation of formation $\boldsymbol{x}$ can be expressed as

$$\boldsymbol{x}^{(k+1)} = \boldsymbol{x}^{(k)} + \boldsymbol{\nu}^{(k)} + \boldsymbol{c}^{(k)} + \mathbf{w}^{(k)}, \tag{5}$$

where

$$\boldsymbol{\nu}^{(k)} = \left[\boldsymbol{u}^{(k)\mathrm{T}}, \boldsymbol{u}^{(k)\mathrm{T}}, \ldots, \boldsymbol{u}^{(k)\mathrm{T}}\right]^{\mathrm{T}}, \tag{6}$$

$$\boldsymbol{c}^{(k)} = \left[\boldsymbol{c}_1^{(k)\mathrm{T}}, \boldsymbol{c}_2^{(k)\mathrm{T}}, \ldots, \boldsymbol{c}_N^{(k)\mathrm{T}}\right]^{\mathrm{T}}, \tag{7}$$

$$\mathbf{w}^{(k)} = \left[\mathbf{w}_1^{(k)\mathrm{T}}, \mathbf{w}_2^{(k)\mathrm{T}}, \ldots, \mathbf{w}_N^{(k)\mathrm{T}}\right]^{\mathrm{T}} \tag{8}$$

are the absolute control vector, the relative control vector, and the control noise of the entire formation, respectively. Denote the covariance matrix of control noise as $\boldsymbol{\Sigma}$.

C. General Framework

In this part, we introduce the general framework of localization and control, as shown in Fig. 2. In each round, the agents take measurements $\mathbf{y}$ to estimate their positions. Then the system compares the current formation $\boldsymbol{x}$ with the target formation $\boldsymbol{\xi}$ to decide control strategies to minimize the formation error. The control strategies contains the globe control strategy to keep the whole formation moving forward together, and the relative control strategy to make the relative formation as close as possible to the target formation. The former is a consensus problem on each absolute move, which can be sloved by consensus algorithms [11]. The latter is an optimization problem to minimize $d(\boldsymbol{\xi}, \boldsymbol{x})$, which is the key problem to be solved in this paper. This process is to maximize formation accuracy based on the available measurements. Besides, there is another important feedback process. The system calculates the influence coefficient of each agent's localization error on the overall formation accuracy, and then the system allocates resources for localization based on these coefficients, to decide what measurements are available in the next round. This process ensures the constrained resources can be used effectively to reduce consumption while maintaining the formation accuracy.

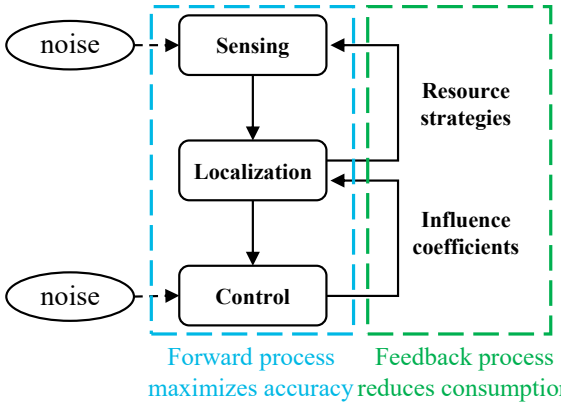

Fig. 2. The general framework for localization and control tasks.

III. Integrated Framework

We establish an integrated localization and control framework for the 3D formation in this section. In part A, we analyze the relative formation error and find its closed upper bound (23) and lower bound (24). In part B, we obtain a closed-form approximate bound (33) of the mean formation error, which shows how the measures errors and control errors influence the formation accuracy. In part C, we propose feedback resource allocation algorithms.

A. Formation Error

For simplification, we assume the center of the target formation $\boldsymbol{\xi}$ is located at the origin. The optimization problem in (3) can be expressed as

$$\min_{\boldsymbol{R}\in\mathrm{SO}(3),\boldsymbol{k}\in\mathbb{R}^3} \|(\boldsymbol{I}\otimes\boldsymbol{R})\boldsymbol{\xi}+\boldsymbol{I}\otimes\boldsymbol{k}-\boldsymbol{x}\|^2. \tag{9}$$

where the optimization variables include translation and rotation. We first deal with the former. Denote the above objective function as $f(\boldsymbol{R},\boldsymbol{k})$ and let the derivative of f with respect to $\boldsymbol{k}$ to equal zero, i.e.

$$\frac{\partial f}{\partial \boldsymbol{k}} = 2(\boldsymbol{k}-\sum_{i=1}^{N}\boldsymbol{x}_i) = 0. \tag{10}$$

Then the optimal $\boldsymbol{k}$ is $\sum_{i=1}^{N}\boldsymbol{x}_i$. If denote $\tilde{\boldsymbol{x}} \triangleq \boldsymbol{x} - (\boldsymbol{1}_N \otimes \sum_{i=1}^{N}\boldsymbol{x}_i)$, which is the formation obtained by translating the center of $\boldsymbol{x}$ to the origin, the original optimization problem can be transformed into

$$\min_{\boldsymbol{R}\in\mathrm{SO}(3)} \sum_{i=1}^{N}\|\boldsymbol{\xi}_i-\boldsymbol{R}\tilde{\boldsymbol{x}}_i\|^2. \tag{11}$$

where the optimization variable only includes rotation. Thus if the center of each formation is translated to the origin, the translation equivalence can be ignored.

Then we deal with the rotation. We use unit quaternions to describe three-dimensional rotations. For a point $\boldsymbol{r}=(a,b,c)$ in three-dimensional space, it corresponds to a quaternion $a\mathrm{i}+b\mathrm{j}+c\mathrm{k}$, where i, j, and k are the basic quaternions. It is also denoted as $\boldsymbol{r}$ without ambiguity. An unit quaternion $\boldsymbol{p}$ corresponds to a 3D rotation, which translates a point $\boldsymbol{r}$ to $\boldsymbol{prp}^*$, where $\boldsymbol{p}^*$ is the conjugation of $\boldsymbol{p}$.

After some straight-forward calculations, we can get the following proposition.

Proposition 1: The formation error between the actual formation $\boldsymbol{x}$ and the target formation $\boldsymbol{\xi}$ can be expressed as

$$d(\boldsymbol{\xi},\boldsymbol{x}) = \|\boldsymbol{\xi}\|^2+\|\tilde{\boldsymbol{x}}\|^2-\lambda_m(\boldsymbol{T}(\boldsymbol{\xi},\tilde{\boldsymbol{x}})), \tag{12}$$

where $\lambda_m(\cdot)$ is the maximum eigenvalue function, $\boldsymbol{T}(\boldsymbol{\xi},\boldsymbol{x}) \triangleq \sum_{i=1}^{N}\boldsymbol{T}_0(\boldsymbol{\xi}_i,\boldsymbol{x}_i)$, and $\boldsymbol{T}_0:\mathbb{R}^3\times\mathbb{R}^3\to\mathbb{R}^{4\times4}$ is a bilinear mapping defined in (13), shown at the bottom of the page.

Proof 1: Using unit quaternions, each term in (11) can be expressed as

$$\|\boldsymbol{\xi}_i-\boldsymbol{p}\tilde{\boldsymbol{x}}_i\boldsymbol{p}^*\|^2 = \|\boldsymbol{\xi}_i\|^2+\|\tilde{\boldsymbol{x}}_i\|^2-\boldsymbol{p}\tilde{\boldsymbol{x}}_i\boldsymbol{p}^*\boldsymbol{\xi}_i-\boldsymbol{p}\boldsymbol{\xi}_i\boldsymbol{p}^*\tilde{\boldsymbol{x}}_i. \tag{14}$$

Regard $\boldsymbol{p}$ as a 4×1 vector and direct calculation shows

$$\boldsymbol{p}\tilde{\boldsymbol{x}}_i\boldsymbol{p}^*\boldsymbol{\xi}_i+\boldsymbol{p}\boldsymbol{\xi}_i\boldsymbol{p}^*\tilde{\boldsymbol{x}}_i = \boldsymbol{p}^\top\boldsymbol{T}_0(\boldsymbol{\xi}_i,\tilde{\boldsymbol{x}}_i)\boldsymbol{p}, \tag{15}$$

which is equivalent to the expression in [12]. Then the optimization problem (11) is equivalent to

$$\min_{\boldsymbol{p}}\sum_{i=1}^{N}\|\boldsymbol{\xi}_i-\boldsymbol{p}\tilde{\boldsymbol{x}}_i\boldsymbol{p}^*\|^2 = \|\boldsymbol{\xi}\|^2+\|\tilde{\boldsymbol{x}}\|^2-\max_{\boldsymbol{p}}\boldsymbol{p}^\top\boldsymbol{T}(\boldsymbol{\xi},\tilde{\boldsymbol{x}})\boldsymbol{p}. \tag{16}$$

Noting that $\|\boldsymbol{p}\|^2=1$, the minimum value of the last item is $-\lambda_m(\boldsymbol{T}(\boldsymbol{\xi},\tilde{\boldsymbol{x}}))$. Then we complete the proof. □

Compared with the 2D formation error [7], the 3D formation error has no closed-form expression. However, we can analyze its upper and lower bounds based on the following facts about $\lambda_m(T(\boldsymbol{\xi},\tilde{\boldsymbol{x}}))$.

Proposition 2: Regard $\lambda_m(T(\boldsymbol{\xi},\boldsymbol{x}))$ as a function of $\boldsymbol{x}$ whose domian is $\mathcal{D}=\{\boldsymbol{x}\in\mathbb{R}^{3N}:\sum_{i=1}^{N}\boldsymbol{x}_i=\boldsymbol{0}\}$. This function has the following properties:

(i) The support set, i.e. $\mathrm{supp}\ \lambda_m(T(\boldsymbol{\xi},\boldsymbol{x})) \triangleq \{\boldsymbol{x}\in\mathcal{D}:\lambda_m(T(\boldsymbol{\xi},\boldsymbol{x}))\neq\boldsymbol{0}\}$, is a subset of $\mathrm{span}(\mathcal{F}_{\boldsymbol{\xi}})$. Besides, $\dim\ \mathrm{supp}\ \lambda_m(T(\boldsymbol{\xi},\boldsymbol{x})) \leqslant \dim\ \mathrm{span}(\mathcal{F}_{\boldsymbol{\xi}}) \leqslant 9$.

(ii) There exists a positive semi-definite matrix $\boldsymbol{H}$ subject to

$$\sqrt{\boldsymbol{x}_{/\!/}^\top\boldsymbol{H}\boldsymbol{x}_{/\!/}} \leqslant \lambda_m(T(\boldsymbol{\xi},\boldsymbol{x})) \leqslant 9\sqrt{\boldsymbol{x}_{/\!/}^\top\boldsymbol{H}\boldsymbol{x}_{/\!/}} \tag{17}$$

where $\boldsymbol{x}_{/\!/}\triangleq\boldsymbol{\Pi}\boldsymbol{x}$, $\boldsymbol{\Pi}\triangleq[\boldsymbol{e}_1,\boldsymbol{e}_2,\cdots,\boldsymbol{e}_m]$, and $\{\boldsymbol{e}_1,\boldsymbol{e}_2,\cdots,\boldsymbol{e}_m\}$ is a set of orthonormal basis of $\mathrm{span}(\mathcal{F}_{\boldsymbol{\xi}})$.

Proof 2:

(i) Noting $\forall\boldsymbol{x}\in\mathcal{D}\cap\mathrm{span}(\mathcal{F}_{\boldsymbol{\xi}})^\perp$, $\|\boldsymbol{x}-(\boldsymbol{I}\otimes\boldsymbol{R})\boldsymbol{\xi}\|^2 = \|\boldsymbol{x}\|^2+\|\boldsymbol{\xi}\|^2$, we have

$$d(\boldsymbol{\xi},\boldsymbol{x}) = \|\boldsymbol{\xi}\|^2+\|\boldsymbol{x}\|^2,\ \forall\boldsymbol{x}\in\mathcal{D}\cap\mathrm{span}(\mathcal{F}_{\boldsymbol{\xi}})^\perp. \tag{18}$$

Comparing this with (12), we have $\lambda_m(T(\boldsymbol{\xi},\boldsymbol{x}))=0$, which implies $\mathrm{supp}\ \lambda_m(T(\boldsymbol{\xi},\boldsymbol{x})) \subseteq \mathrm{span}(\mathcal{F}_{\boldsymbol{\xi}})$ and $\dim\ \mathrm{supp}\ \lambda_m(T(\boldsymbol{\xi},\boldsymbol{x})) \leqslant \dim\ \mathrm{span}(\mathcal{F}_{\boldsymbol{\xi}})$. Besides, we can easily find 9 elements $\boldsymbol{R}_1,\boldsymbol{R}_2,\cdots,\boldsymbol{R}_9\in\mathrm{SO}(3)$, which are linearly independent. Thus they forms a basis of $\mathrm{SO}(3)$. Furthermore, define $\boldsymbol{\xi}_i\triangleq(\boldsymbol{I}\otimes\boldsymbol{R}_i)\boldsymbol{\xi}$, $1\leqslant i\leqslant 9$. For all $\boldsymbol{s}=(\boldsymbol{I}\otimes\boldsymbol{R})\boldsymbol{\xi}$, $\boldsymbol{R}\in\mathrm{SO}(3)$, there exist coefficients $a_1,a_2,\cdots,a_9\in\mathbb{R}$ satisfying

$$\boldsymbol{s} = (\boldsymbol{I}\otimes\sum_{i=1}^{9}a_i\boldsymbol{R}_i)\boldsymbol{\xi} = \sum_{i=1}^{9}a_i\boldsymbol{\xi}_i. \tag{19}$$

This means $\mathrm{span}(\mathcal{F}_{\boldsymbol{\xi}}) = \mathrm{span}(\{\boldsymbol{\xi}_i:1\leqslant i\leqslant 9\})$. Thus we have $\dim\ \mathrm{span}(\mathcal{F}_{\boldsymbol{\xi}})\leqslant 9$.

$$\boldsymbol{T}_0\left(\begin{bmatrix}a_1\\a_2\\a_3\end{bmatrix},\begin{bmatrix}b_1\\b_2\\b_3\end{bmatrix}\right) \triangleq \begin{bmatrix}-a_1b_1-a_2b_2-a_3b_3 & -a_2b_3+a_3b_2 & a_1b_3-a_3b_1 & -a_1b_2+a_2b_1\\ -a_2b_3+a_3b_2 & a_2b_2-a_1b_1+a_3b_3 & -a_1b_2-a_2b_1 & -a_1b_3-a_3b_1\\ a_1b_3-a_3b_1 & -a_1b_2-a_2b_1 & a_1b_1-a_2b_2+a_3b_3 & -a_2b_3-a_3b_2\\ -a_1b_2+a_2b_1 & -a_1b_3-a_3b_1 & -a_2b_3-a_3b_2 & a_1b_1+a_2b_2-a_3b_3\end{bmatrix} \tag{13}$$

(ii) Since $\lambda_m(\boldsymbol{T}(\boldsymbol{\xi},\boldsymbol{x}))$ is a linear function of $\boldsymbol{x}$ and $\lambda_m(\cdot)$ is convex, the set $B \triangleq \{\boldsymbol{p}\in\mathcal{D}:\lambda_m(T(\boldsymbol{\xi},\boldsymbol{p}))\leqslant 1\}$ is convex. Thus among all hyperellipsoids containing B, there exists a unique ellipsoid $E_{\mathrm{m}}=\{\boldsymbol{p}:\sqrt{\boldsymbol{p}^\top\boldsymbol{\Pi}^\top\boldsymbol{H}\boldsymbol{\Pi}\boldsymbol{p}}\leqslant 1\}$ of the minimum volume, called the Löwner-John ellipsoid [13], satisfying

$$\frac{1}{9}E_{\mathrm{m}}\subseteq\frac{1}{\dim\ B}E_{\mathrm{m}}\subseteq B\subseteq E_{\mathrm{m}}. \tag{20}$$

Thus we have $\forall\boldsymbol{p}\in\bar{B}=\{\boldsymbol{p}\in\mathcal{D}:\lambda_m(T(\boldsymbol{\xi},\boldsymbol{p}))=1)\}$,

$$\sqrt{\boldsymbol{p}_{/\!/}^\top\boldsymbol{H}\boldsymbol{p}_{/\!/}}\leqslant\lambda_m(\boldsymbol{T}(\boldsymbol{\xi},\boldsymbol{p}))\leqslant 9\sqrt{\boldsymbol{p}_{/\!/}^\top\boldsymbol{H}\boldsymbol{p}_{/\!/}} \tag{21}$$

where the subscript $/\!/$ means the projection to $\mathrm{span}(\mathcal{F}_{\boldsymbol{\xi}})$. Furthermore, $\forall\boldsymbol{q}\in\mathcal{D}$, denote $\nu=\lambda_m(T(\boldsymbol{\xi},\boldsymbol{q}))$ and $\boldsymbol{r}=\frac{1}{\nu}\boldsymbol{q}$, then $\boldsymbol{r}\in\bar{B}$ satisfies (21). By multiplying each side of the inequality by ν, and noting $\nu\lambda_m(\boldsymbol{T}(\boldsymbol{\xi},\boldsymbol{r}))=\lambda_m(\boldsymbol{T}(\boldsymbol{\xi},\nu\boldsymbol{r}))=\lambda_m(\boldsymbol{T}(\boldsymbol{\xi},\boldsymbol{q}))$, we know the arbitrary point $\boldsymbol{q}$ also satisfies (21). □

Combining (12) and (17), we can further get the closed-form upper bound and lower bound of the mean formation error as follows

$$\underline{d}(\boldsymbol{\xi},\boldsymbol{x})\leqslant d(\boldsymbol{\xi},\boldsymbol{x})\leqslant\overline{d}(\boldsymbol{\xi},\boldsymbol{x}). \tag{22}$$

where

$$\underline{d}(\boldsymbol{\xi},\boldsymbol{x})=\max\left\{\|\boldsymbol{\xi}\|^2+\|\tilde{\boldsymbol{x}}\|^2-9\sqrt{\tilde{\boldsymbol{x}}_{/\!/}^\top\boldsymbol{H}\tilde{\boldsymbol{x}}_{/\!/}},0\right\}, \tag{23}$$

$$\overline{d}(\boldsymbol{\xi},\boldsymbol{x})=\|\boldsymbol{\xi}\|^2+\|\tilde{\boldsymbol{x}}\|^2-\sqrt{\tilde{\boldsymbol{x}}_{/\!/}^\top\boldsymbol{H}\tilde{\boldsymbol{x}}_{/\!/}}. \tag{24}$$

Remark 1: The difference between the bounds and the true value is bounded by $8\sqrt{\tilde{\boldsymbol{x}}_{/\!/}^\top\boldsymbol{H}\tilde{\boldsymbol{x}}_{/\!/}}$, which is approximately proportional to the formation scale. Besides, the upper bound is tighter than the lower bound since we use the minimum volume hyperellipsoid containing B to derive the bounds. We can also use the maximum volume hyperellipsoid contained in B to derive a tighter lower bound with a similar form.

B. Formation Error Limit

Since the formation error $d(\boldsymbol{\xi},\boldsymbol{x})$ has no closed-form expression, we next analyze its upper bound $\overline{d}(\boldsymbol{\xi},\boldsymbol{x})$. Suppose the control algorithm is unbiased, i.e. there exists $\boldsymbol{s}\in\mathcal{F}_{\boldsymbol{\xi}}$ subject to $\mathbb{E}[\boldsymbol{x}+\boldsymbol{c}(\mathbf{y})+\mathbf{n}]=\boldsymbol{s}$.

Compute the second-order Taylor series expansion of $\sqrt{\tilde{\boldsymbol{x}}_{/\!/}^\top\boldsymbol{H}\tilde{\boldsymbol{x}}_{/\!/}}$ around $\tilde{\boldsymbol{s}}$ and we have

$$\begin{aligned}\sqrt{\tilde{\boldsymbol{x}}_{/\!/}^\top\boldsymbol{H}\tilde{\boldsymbol{x}}_{/\!/}}=&\sqrt{\tilde{\boldsymbol{s}}_{/\!/}^\top\boldsymbol{H}\tilde{\boldsymbol{s}}_{/\!/}}+\frac{\tilde{\boldsymbol{s}}_{/\!/}^\top\boldsymbol{H}(\tilde{\boldsymbol{x}}_{/\!/}-\tilde{\boldsymbol{s}}_{/\!/})}{\sqrt{\tilde{\boldsymbol{s}}_{/\!/}^\top\boldsymbol{H}\tilde{\boldsymbol{s}}_{/\!/}}}\\&+(\tilde{\boldsymbol{x}}_{/\!/}-\tilde{\boldsymbol{s}}_{/\!/})^\top\tilde{\boldsymbol{H}}(\tilde{\boldsymbol{x}}_{/\!/}-\tilde{\boldsymbol{s}}_{/\!/})+\cdots\end{aligned} \tag{25}$$

where $\tilde{\boldsymbol{H}}=\frac{1}{2}\left(\frac{\boldsymbol{H}}{\sqrt{\tilde{\boldsymbol{s}}_{/\!/}^\top\boldsymbol{H}\tilde{\boldsymbol{s}}_{/\!/}}}-\frac{\boldsymbol{H}\tilde{\boldsymbol{s}}_{/\!/}\tilde{\boldsymbol{s}}_{/\!/}^\top\boldsymbol{H}}{(\tilde{\boldsymbol{s}}_{/\!/}^\top\boldsymbol{H}\tilde{\boldsymbol{s}}_{/\!/})^{\frac{3}{2}}}\right)$. Since noise is usually very small, the higher-order infinitesimals can be ignored. Taking (25) into $\overline{d}(\boldsymbol{\xi},\boldsymbol{x}+\boldsymbol{c}(\mathbf{y})+\mathbf{n})$ and taking expectations on both sides, we can get

$$\begin{aligned}\mathbb{E}[d(\boldsymbol{\xi},\boldsymbol{x}^+)]=&\mathbb{E}\|\tilde{\boldsymbol{x}}_\perp^+\|^2+\mathbb{E}[(\tilde{\boldsymbol{x}}_{/\!/}^+-\tilde{\boldsymbol{s}}_{/\!/})^\top(\boldsymbol{I}-\tilde{\boldsymbol{H}})(\tilde{\boldsymbol{x}}_{/\!/}^+-\tilde{\boldsymbol{s}}_{/\!/})]\\&+\|\boldsymbol{\xi}\|^2+\|\boldsymbol{s}\|^2-\sqrt{\tilde{\boldsymbol{s}}_{/\!/}^\top\boldsymbol{H}\tilde{\boldsymbol{s}}_{/\!/}}\\&+\text{higher-order terms}\end{aligned} \tag{26}$$

where $\boldsymbol{x}^+\triangleq\boldsymbol{x}+\boldsymbol{c}(\mathbf{y})+\mathbf{n}$ and the subscript $\perp$ is the projection to $\mathrm{span}(\mathcal{F}_{\boldsymbol{\xi}})^\perp$. The first two terms on the right have lower bounds as follows.

Proposition 3: Under the aforementioned notations, there are the following conclusions.

(i) $\mathbb{E}\|\tilde{\boldsymbol{x}}_\perp^+\|^2\ \geqslant\ \mathrm{tr}\left\{(\boldsymbol{I}-\boldsymbol{\Pi}\boldsymbol{\Pi}^\top)(\boldsymbol{J}^{-1}+\boldsymbol{\Sigma})\right\}$ where the equality holds if

$$\tilde{\boldsymbol{c}}_\perp(\mathbf{y})=-\tilde{\boldsymbol{x}}_\perp+\boldsymbol{\Pi}^\perp\boldsymbol{J}^{-1}\frac{\partial}{\partial\boldsymbol{x}}\ln p(\mathbf{y};\boldsymbol{x}) \tag{27}$$

where $\boldsymbol{\Pi}^\perp$ is the orthogonal complement of $\boldsymbol{\Pi}$.

(ii) $\mathbb{E}[(\tilde{\boldsymbol{x}}_{/\!/}^+-\tilde{\boldsymbol{s}}_{/\!/})^\top(\boldsymbol{I}-\tilde{\boldsymbol{H}})(\tilde{\boldsymbol{x}}_{/\!/}^+-\tilde{\boldsymbol{s}}_{/\!/})]\ \geqslant\ \mathrm{tr}\{(\boldsymbol{I}-\tilde{\boldsymbol{H}})\boldsymbol{\Pi}(\boldsymbol{J}^{-1}+\boldsymbol{\Sigma})\boldsymbol{\Pi}^\top\}$ where the equality holds if

$$\tilde{\boldsymbol{c}}_{/\!/}(\mathbf{y})=\tilde{\boldsymbol{s}}_{/\!/}-\tilde{\boldsymbol{x}}_{/\!/}+\boldsymbol{U}\boldsymbol{\Pi}\boldsymbol{J}^{-1}\frac{\partial}{\partial\boldsymbol{x}}\ln p(\mathbf{y};\boldsymbol{x}). \tag{28}$$

Proof 3: We firstly prove (ii). Decompose $\boldsymbol{I}-\tilde{\boldsymbol{H}}$ into $\boldsymbol{U}^\top\boldsymbol{U}$ and define $\boldsymbol{e}(\mathbf{y})\triangleq\boldsymbol{U}(\tilde{\boldsymbol{x}}_{/\!/}+\tilde{\boldsymbol{c}}_{/\!/}(\mathbf{y})-\tilde{\boldsymbol{s}}_{/\!/})$, then the left side of the inequality can be expressed as

$$\mathbb{E}[\boldsymbol{e}(\mathbf{y})^\top\boldsymbol{e}(\mathbf{y})]+\mathrm{tr}\{(\boldsymbol{I}-\tilde{\boldsymbol{H}})\boldsymbol{\Pi}\boldsymbol{\Sigma}\boldsymbol{\Pi}^\top\}. \tag{29}$$

Denote $\Delta\triangleq\frac{\partial}{\partial\boldsymbol{x}}\ln p(\mathbf{y};\boldsymbol{x})$. For any $\boldsymbol{W}\in\mathbb{R}^{9\times 3N}$, we have

$$\mathbb{E}[(\boldsymbol{e}(\mathbf{y})-\boldsymbol{W}\Delta)(\boldsymbol{e}(\mathbf{y})-\boldsymbol{W}\Delta)^\top]\succeq\mathbf{0} \tag{30}$$

which can be transformed into

$$\begin{aligned}\mathbb{E}[\boldsymbol{e}(\mathbf{y})\boldsymbol{e}(\mathbf{y})^\top]\succeq&\boldsymbol{U}\boldsymbol{\Pi}\boldsymbol{J}^{-1}\boldsymbol{\Pi}^\top\boldsymbol{U}^\top\\&-(\boldsymbol{W}-\boldsymbol{U}\boldsymbol{\Pi}\boldsymbol{J}^{-1})\boldsymbol{J}(\boldsymbol{W}-\boldsymbol{U}\boldsymbol{\Pi}\boldsymbol{J}^{-1})^\top.\end{aligned} \tag{31}$$

Due to the arbitrariness of $\boldsymbol{W}$, we can get

$$\mathbb{E}[\boldsymbol{e}(\mathbf{y})^\top\boldsymbol{e}(\mathbf{y})]\geqslant\mathrm{tr}\{(\boldsymbol{I}-\tilde{\boldsymbol{H}})\boldsymbol{\Pi}\boldsymbol{J}^{-1}\boldsymbol{\Pi}^\top\}. \tag{32}$$

Combining with (29), we can get the conclusion (ii). Conclusion (i) can be simply obtained by a similar process. □

Remark 2: (27) and (28) provide an optimal control algorithm. In the implementation, we can replace the actual formation with the estimated formation and the term $\frac{\partial}{\partial\boldsymbol{x}}\ln p(\mathbf{y};\boldsymbol{x})$ can be calculated numerically by the method in [7].

We finally get the core conclusion of this section, the closed-form approximate lower bound of $\mathbb{E}[\overline{d}(\boldsymbol{\xi},\boldsymbol{x}^+)]$, as follows

$$\begin{aligned}\mathbb{E}[\overline{d}(\boldsymbol{\xi},\boldsymbol{x}^+)]\gtrsim&\mathrm{tr}\left\{(\boldsymbol{I}-\boldsymbol{\Pi}\boldsymbol{\Pi}^\top)(\boldsymbol{J}^{-1}+\boldsymbol{\Sigma})\right\}\\&+\mathrm{tr}\left\{(\boldsymbol{I}-\tilde{\boldsymbol{H}})\boldsymbol{\Pi}(\boldsymbol{J}^{-1}+\boldsymbol{\Sigma})\boldsymbol{\Pi}^\top\right\}\\&+\|\boldsymbol{\xi}\|^2+\|\boldsymbol{s}\|^2-\sqrt{\tilde{\boldsymbol{s}}_{/\!/}^\top\boldsymbol{H}\tilde{\boldsymbol{s}}_{/\!/}}.\end{aligned} \tag{33}$$

The first two terms on the right are the lower bounds of mean formation error projected to $\mathrm{span}(\mathcal{F}_{\boldsymbol{\xi}})^\perp$ and $\mathrm{span}(\mathcal{F}_{\boldsymbol{\xi}})$, respectively. The sum of the other terms is a constant near 0 since it is the upper bound approximation of $d(\boldsymbol{\xi},\boldsymbol{s})$ which is 0.

C. Resource Allocation

(33) characterizes how the measurement information influences formation accuracy under complex coupling relationships. It provides a way to reasonably allocate limited resources to improve accuracy. Since the position error of different agents affects the formation accuracy differently, we can use the following weights to quantitatively describe it,

$$w_i = \mathrm{tr}\left\{\frac{\partial \min \mathbb{E}[\bar{d}(\boldsymbol{\xi}, \mathbf{x})]}{\partial (\boldsymbol{J}^{-1})_{ii}}\right\} \tag{34}$$

where $(\boldsymbol{J}^{-1})_{ii}$ is the i-th 3×3 submatrix that starts from element $3(i-1)+1$ on the diagonal of $\boldsymbol{J}^{-1}$. This describes how much the formation accuracy can be improved by increasing an unit localization accuracy of agent i.

In specific issues, we can combine the information update process to obtain more refined weights. Consider such a filtering process. The Fisher information matrix of a formation $\boldsymbol{x}$ at time k is $\boldsymbol{J}_k$ and the measurement information matrix at time k is $\Delta \boldsymbol{J}_k$. Besides, the covariance matrix of motion noise is $\boldsymbol{\Sigma}_k$. The Fisher information matrix $\boldsymbol{J}_k$ update process can be described as [14]

$$\boldsymbol{J}_{k+1}^{-1} = (\boldsymbol{J}_k + \Delta \boldsymbol{J}_k)^{-1} + \boldsymbol{\Sigma}_k \tag{35}$$

We use the following weights to precisely describe the impact of each measurement on the formation accuracy.

$$w_i = \mathrm{tr}\left\{\frac{\partial \min \mathbb{E}[\bar{d}(\boldsymbol{\xi}, \mathbf{x})]}{\partial (\Delta \boldsymbol{J})_{ii}}\right\} \tag{36}$$

Based on these discussions, we can implement agent scheduling and resource allocation in a tightly coupled way. For agent scheduling problems, assume that n agents can be measured at each time. We can greedily choose the n agents with the highest weights as follows to ensure that resources are used to the most valuable agents.

$$\{i_1, i_2, \cdots, i_n\} = \underset{\{i_1, i_2, \cdots, i_n\} \subseteq \{1,2,\cdots,N\}}{\arg\max} \sum_{k=1}^{n} w_{i_k} \tag{37}$$

For power allocation problems, suppose the total power is P_{total} and consider the ranging model with anchors where the measurement information is proportional to the signal power [15]. To improve the resource utilization efficiency, we can allocate the power based on the weights $\{w_i\}$, i.e. the power of agent i is allocated as

$$P_i = \frac{w_i}{\sum_{j=1}^{N} w_j} P_{\mathrm{total}} \tag{38}$$

This ensures that most of the power is effectively used to improve formation accuracy.

We will compare our proposed algorithms in the next section to show the superiority of the integrated design.

IV. Numerical Results

In this section, we use numerical experiments to compare the bounds and the true value of formation errors, and verify the performance of the proposed algorithms.

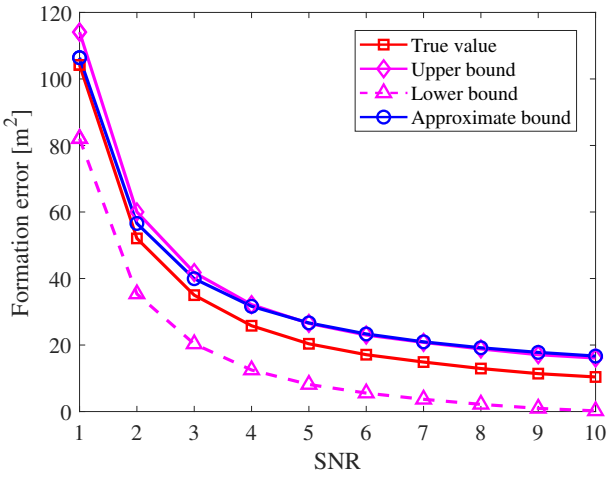

Fig. 3. The numerical values of mean formation error and its bounds. The red line and purple lines are calculated by the Monte Carlo method. The proposed bound (blue line) approximates the upper bound well.

A. Theoretical bound

Firstly, we numerically compare the mean formation error $\mathbb{E}[d(\boldsymbol{\xi}, \mathbf{x})]$, its upper bound $\mathbb{E}[\bar{d}(\boldsymbol{\xi}, \mathbf{x})]$, its lower bound $\mathbb{E}[\underline{d}(\boldsymbol{\xi}, \mathbf{x})]$, and the approximate bound (33). Although the first three items have no closed expressions, they can be calculated by the Monte Carlo method. Consider an 8-agent cube formation with a side length of 2m. Each agent is located on a vertex of the cube. The corresponding matrix $\boldsymbol{H}$ can be calculated by minimum volume enclosing ellipsoid methods [16]. Suppose the measurement process is direct measurement and the localization errors of agents are isotropic and identical. The control noises of agents are independent and identically distributed random variables with the Gaussian distribution $\mathcal{N}(\mathbf{0}, \sigma^2 \boldsymbol{I})$, where $\sigma = 0.2\mathrm{m}$. The numerical results are shown in Fig. 3. It can be seen that the upper and lower bounds well reflect the trend of the true value, and the approximate bound (33) is close to the Monte Carlo result.

B. Agent scheduling

In order to compare different algorithms more effectively, we consider a 20-agent formation scenery now. We randomly select 20 points in a cube with a side length of 100m as the target formation $\boldsymbol{\xi}$. For each round, only n agents can be measured simultaneously due to resource constraints, where n varies from 2 to 20. We compare the proposed algorithm described as (37) with the random scheduling algorithm and the sequential scheduling algorithm. The random scheduling algorithm randomly selects n agents at each time and the sequential algorithm selects n agents in sequence. The mean formation errors for three algorithms at steady state are shown in Fig. 4. It shows that with the same number of scheduling agents, the proposed algorithm can greatly reduce the mean formation error. On the other hand, the proposed algorithm can achieve the same formation accuracy with only a small amount of scheduling. This is because the proposed algorithm

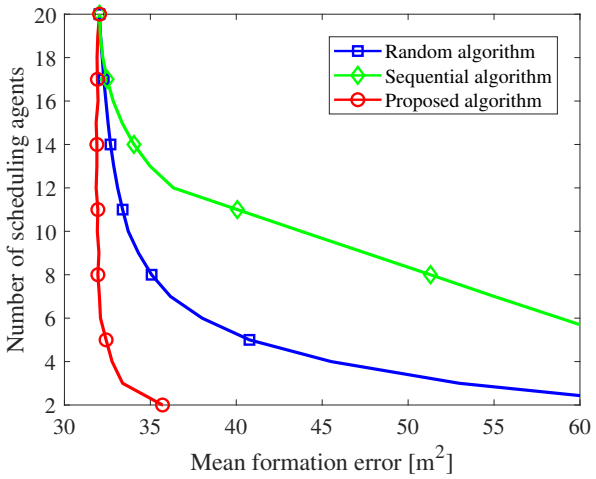

Fig. 4. The number of scheduling agents needed by different scheduling algorithms to achieve the same mean formation error. The proposed algorithm (red line) greatly reduces the number of scheduling.

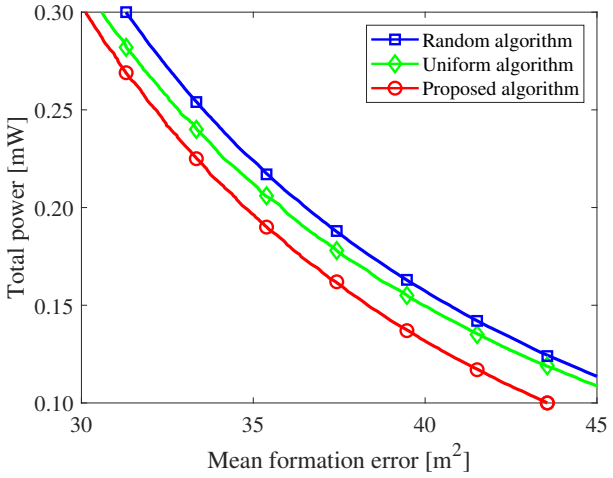

Fig. 5. The total power needed by different power allocation algorithms to achieve the same mean formation error. The proposed algorithm (red line) effectively reduces energy consumption.

effectively evaluates the impact of scheduling on the formation accuracy gain so that the resources are fully utilized.

C. Power allocation

Suppose the total power available to all agents for measurement is limited and the total power varies from $0.1\mathrm{mW}$ to $0.3\mathrm{mW}$. The remaining parameters are the same as in part B. We compare the proposed algorithm described as (38) with the random algorithm and the uniform algorithm, and the mean formation errors at steady states are shown in Fig. 5. It shows that the proposed algorithm can reduce the total power by $10\% \sim 20\%$ while achieving the same formation accuracy. Especially under low power conditions, the proposed algorithm has greater gain. On the other hand, under the same power, the proposed algorithm can also reduce the mean formation error by about 10%. These results show that the proposed algorithm is of great help in reducing energy consumption.

V. Conclusion

In this paper, we establish an integrated localization and control framework for the 3D formation. Firstly, we analyze the relative formation error and find the closed upper and lower bounds of the mean formation error. Secondly, we analyze the bound of formation accuracy under any unbiased control algorithm and provide a closed-form approximate upper bound, which shows how the measurement errors and control errors influence the formation accuracy. Finally, we propose feedback resource allocation algorithms based on the integrated framework. The simulation experiments verify the significant performance gain and resource cost reduction obtained by the integrated design.

Acknowledgment

This research was supported in part, by Basic Research Strengthening Program of China (173 Program) (2020-JCJQ-ZD-015-01) and Tsinghua University - Meituan Joint Institute for Digital Life.

References

[1] K. Gu, Y. Wang, and Y. Shen, "Cooperative detection by multi-agent networks in the presence of position uncertainty," *IEEE Trans. Signal Process.*, vol. 68, pp. 5411–5426, Sep. 2020.
[2] S. Zhang, R. Pöhlmann, T. Wiedemann, A. Dammann, H. Wymeersch, and P. A. Hoeher, "Self-aware swarm navigation in autonomous exploration missions," *Proc. IEEE*, vol. 108, no. 7, pp. 1168–1195, Jul. 2020.
[3] A. Sen, M. Kothari, and S. R. Sahoo, "Information-rich formation tracking: a unified scheme of cooperative control and localization," *J. Aerosp. Inform. Syst.*, vol. 17, no. 8, pp. 390–406, Apr. 2020.
[4] K. K. Oh, M. C. Park, and H. S. Ahn, "A survey of multi-agent formation control," *Automatica.*, vol. 53, no. s, pp. 424–440, Mar. 2015.
[5] S.-H. Kwon, Z. Sun, B. Anderson, and H.-S. Ahn, "Hybrid distance-angle rigidity theory with signed constraints and its applications to formation shape control," *arXiv preprint arXiv:1912.12952*, 2019.
[6] P. H. Schönemann and R. M. Carroll, "Fitting one matrix to another under choice of a central dilation and rigid motion," *Psychometrika*, vol. 35, no. 2, pp. 245–255, Jun. 1970.
[7] Y. Cai and Y. Shen, "An integrated localization and control framework for multi-agent formation," *IEEE Trans. Signal Process.*, vol. 67, no. 7, pp. 1941 – 1956, Apr. 2019.
[8] Z. Han, K. Guo, L. Xie, and Z. Lin, "Integrated relative localization and leader–follower formation control," *IEEE Trans. Autom. Control*, vol. 64, no. 1, pp. 20–34, Feb. 2019.
[9] K. Ma and Y. Shen, "Distributed formation algorithm based on integrated localization and control," in *Proc. IEEE Global Commun. Conf.*, Taipei, China, Dec. 2020, pp. 1–5.
[10] B. D. Anderson, C. Yu, B. Fidan, and J. M. Hendrickx, "Rigid graph control architectures for autonomous formations," *IEEE Control Syst. Mag.*, vol. 28, no. 6, pp. 48–63, Dec. 2008.
[11] W. Ren, R. W. Beard, and E. M. Atkins, "A survey of consensus problems in multi-agent coordination," in *Proc. Am. Control Conf.*, Portland, USA, Jun. 2005, pp. 1–6.
[12] B. K. Horn, "Closed-form solution of absolute orientation using unit quaternions," *Josa a*, vol. 4, no. 4, pp. 629–642, Apr. 1987.
[13] M. Henk, "löwner-john ellipsoids," *Documenta Math*, vol. 95, p. 106, 2012.
[14] T. Wang, Y. Shen, A. Conti, and M. Z. Win, "Network navigation with scheduling: Error evolution," *IEEE Trans. Inf. Theory*, vol. 63, no. 11, pp. 7509–7534, Nov. 2017.
[15] M. Z. Win, Y. Shen, and W. Dai, "A theoretical foundation of network localization and navigation," *Proc. IEEE*, vol. 106, no. 7, pp. 1136–1165, Jul. 2018.
[16] S. Silvey, *Optimal design: an introduction to the theory for parameter estimation*. New York: Springer Science & Business Media, 2013.